

ARCHIVIO ISTITUZIONALE
DELLA RICERCA

Alma Mater Studiorum Università di Bologna
Archivio istituzionale della ricerca

An open database for benchmarking guided waves structural health monitoring algorithms on a composite full-scale outer wing demonstrator

This is the final peer-reviewed author's accepted manuscript (postprint) of the following publication:

*Published Version:*
Marzani, A., Testoni, N., De Marchi, L., Messina, M., Monaco, E., Apicella, A. (2020). An open database for benchmarking guided waves structural health monitoring algorithms on a composite full-scale outer wing demonstrator. STRUCTURAL HEALTH MONITORING, 2019(5), 1524-1541 [10.1177/1475921719889029].

*Availability:*
This version is available at: https://hdl.handle.net/11585/707123 since: 2020-08-07

*Published:*

DOI: http://doi.org/10.1177/1475921719889029

*Terms of use:*

Some rights reserved. The terms and conditions for the reuse of this version of the manuscript are specified in the publishing policy. For all terms of use and more information see the publisher's website.

This item was downloaded from IRIS Università di Bologna (https://cris.unibo.it/).
When citing, please refer to the published version.

(Article begins on next page)

21 November 2026

Journal Title
XX(X):1–15
©The Author(s) 2018
Reprints and permission:
sagepub.co.uk/journalsPermissions.nav
DOI: 10.1177/ToBeAssigned
www.sagepub.com/
SAGE

# An open database for benchmarking guided waves SHM algorithms on a composite full scale outer wing demonstrator

**Alessandro Marzani[1,3], Nicola Testoni[2,3], Luca De Marchi[2,3], Marco Messina[3], Ernesto Monaco[4] and Alfonso Apicella[5]**

**Abstract**

This paper reports on the creation of an open database of piezo-actuated and -received guided waves signals propagating in a composite panel of a full scale aeronautical structure. The composite panel closes the bottom part of a wingbox that, along with the leading edge, the trailing edge and the wingtip, forms an outer wing demonstrator approximately 4.5 meters long and from 1.2 to 2.3 meters wide.

To create the database a Structural Health Monitoring (SHM) system, composed by a software/hardware central unit capable to control a network of 160 piezoelectric transducers secondary bonded on the composite panel, has been realized. The SHM system has been designed to (i) perform electromechanical impedance (EMI) measurement at each transducer, in order to check for their reliability and bonding strength, and (ii) to operate an active guided waves (GW) screening for damage detection in the composite panel.

EMI and GW measurements were performed at four different testing stages: before loading, before fatigue, before impacts, and after impacts. The database, freely available at http://shm.ing.unibo.it/, can thus be used to benchmarking, on real scale structural data, guided waves algorithms for loading, fatigue as well as damage detection, characterization and sizing. As an example, in the work a delay and sum algorithm is applied on the post-impact data to illustrate how the database can be exploited.

**Keywords**

electromechanical impedance, guided waves, fatigue, impacts, composite structures

## Introduction

Composite materials are subjected to an increasing importance in complex structures commonly found in the modern-day industrial, civil and military field, and mostly aviation. The possibility to build structures with a high strength to weight ratio and poorly sensitive to fatigue and corrosion constitutes the greatest advantage of composite materials and boost their usage in aeronautics.

Most of the concern in the use of composites in aeronautics is related to the so-called Barely Visible Impact Damages (BVID), generally originated by impacts, mainly delaminations, which are considered to be particularly dangerous as they can cause structural issues even before becoming visible to the human eye. For this reason the growth in the use of composites in aeronautics walks in parallel with the development of non-destructive approaches for early detection of hidden delaminations. In this context, elastic guided waves (GW) play a major role as they (i) allow for fast inspection of plate-like composite structures, whose large area would make visual and classical trough-thickness ultrasonic inspection unfeasible or unpractical; (ii) are capable to probe the entire volume of the component under inspection; (iii) can be tuned to be sensitive to multiple type of damages and (iv) can lead, in the near future, to embedded systems for in-flight monitoring.

The key operating principle of GW damage monitoring is that delaminations work as wave scatters, giving birth to GW reflections and mode conversion, thus modifying the wave propagation pattern[1]. Combining this with the high speed of propagation, the limited attenuation and the sensitivity to multiple types of damage, including hidden delaminations[2–4], ultrasonic GW are the ideal candidate for damage detection in large structures.

From an operative point of view, arrays of piezoelectric transducers (known as network) are rigidly bonded to the structure to actuate and detect GW propagating within

[1]Department of Civil, Chemical, Environmental and Materials Engineering (DICAM), University of Bologna, Viale del Risorgimento 2, 40136, Bologna, Italy
[2]Department of Electrical, Electronic and Information Engineering (DEI), University of Bologna, Viale del Risorgimento 2, 40136, Bologna, Italy
[3]Advanced Research Center on Electronic Systems "Ercole De Castro" (ARCES), University of Bologna, Via V. Toffano 2/2, 40125, Bologna, Italy
[4]Department of Industrial Engineering - University of Napoli "Federico II" - Via Claudio 21 - 80125, Napoli, Italy
[5]Leonardo S.p.A., Viale dell'Aeronautica, 80038, Pomigliano d'Arco (NA), Italy

**Corresponding author:**
Alessandro Marzani, Department of Civil, Chemical, Environmental and Materials Engineering (DICAM), University of Bologna, Viale del Risorgimento 2, 40136, Bologna, Italy.
Email: alessandro.marzani@unibo.it

the structural component. If a delamination scatter the propagating GW, it can be detected and located in almost real-time by processing the signals recorded from the transducers with proper algorithms (see e.g. Refs.[5–7]). In addition the reduced dimensions, low weight and cost, of the transducers have the potential to allow for the deployment of embedded monitoring systems.

However, to date, SHM approaches based on GW have been mainly developed and tested at laboratory scale and their integration into real operative structures seems still far to come. This is mainly due to some methodological and technological limitations that laboratory scale systems encounter, especially in the aeronautical field, trying to meet the standards needed to monitor real scale applications.

Among the several, the major limitations are:

- the developed signal processing methodologies for impact/damage detection, localization and characterization allow to operate on isotropic and regular geometries, whereas their reliability on composite structures with the presence of stiffeners, rivets, manholes, and other geometrical anomalies, has still to be proven;
- the majority of the developed methodologies need baseline measurements whereas it has been proven that the baseline might change because of temperature, moisture, operative loads, aging, etc.;
- the SHM system technology scalability from laboratories to aircrafts is still unproven, with open issues related to weight, hardware power consumption, power supply limitation, complex circuitry, life duration, and bulky signal processing equipment;
- a fundamental absence of means to comprehensively asses the SHM cost/benefit analysis.

The research community operating in the development of SHM systems is actively involved in analyzing and then addressing all these issues.

For instance, the compensation for effects induced by temperature variations has been thoroughly investigated in Refs.[8–10].

In Ref.[11], a categorization of the existing GW based methods and techniques was provided as a necessary step for bringing SHM into industrial applications via classification and knowledge distribution.

In Ref.[12] the results of a Canadian project, aimed at the creation of a list of elementary components (commonly adopted in aerostructures) and suitable to be inspected with GW methods were presented. In other words, the objective was to define a set of standards, from which the applicability of GW inspection methods for other specific structures could be extrapolated. The list was enriched with information related to the characteristics of GW propagation in such components (in terms of velocity dispersion curves and attenuation) and their interaction with geometrical or damage features.

The work in Ref.[13] presents a way to implement the required Validation and Verification (V&V) strategy to put in place a flight demonstration of a SHM system in a military aeronautical context.

The application of GW inspection methods to structures of high geometric or material complexity were investigated in Ref.[14], while the limited reliability of baseline-based approached was highlighted in Ref.[15].

However, even if many studies were conducted on the development of SHM systems, the lack of a proven strategy for technology up-scaling from laboratory test cases to real-field applications is still relevant[16,17].

Recently, Moll and co-workers[18] introduced an extendable online platform (http://www.open-guided-waves.de) where, among others, high-quality and well documented guided waves signals actuated and received by piezoelectric transducers in a quasi-isotropic carbon-fiber-reinforced plate are available. Their idea is to overcome the limitation of current research due to the lack of freely available benchmark measurements to comparatively evaluate existing methodologies. The database in Ref.[18] is related to simple rectangular coupons, kept at constant temperature, unloaded, and defects are simulated with aluminium disks taped to the composite materials.

The current work's aim is to complement the work by Moll and co-workers[18] by providing to the research community a database which is more closely related to on-field applications. The database here proposed is the output of a SHM system developed within a large scale FP7 European Project named "Smart Intelligent Aircraft Structures - SARISTU"[19].

The database collects electromechanical impedance (EMI) and guided waves (GW) signals acquired on a real aeronautical structure in different testing conditions.

In particular, EMI and GW data were initially acquired on the pristine composite panel, after the panel was assembled into the wingbox and hanged to a metal frame in cantilever configuration, after a severe 90000 cycle aeronautical fatigue testing protocol, and finally after am impact testing protocol in which an air-gun was used to induced delaminations.

As such, the aim of this paper is twofold: (i) to describe the characteristics of an open database obtained from a complex structure under different conditions, that can be used by EMI and GW practitioners to test and validate their own approaches for transducers integrity/coupling as well as defect detection and localization procedures; and (ii) to further highlight common problems emerging while scaling typical GW based SHM laboratory systems to real scale problems.

Regarding point (i), the flexibility of the database allows to process the data in a consistent way and to compare the results of different processing methods on the same experimental platform. Moreover, by making use of a high number of piezoelectric transducers, it makes possible to evaluate the robustness of signal processing methods by varying the number and position of the transducers, looking for instance at the effects of damaged sensors, and test sensor's position optimization procedures as those presented in Refs.[20,21].

Regarding point (ii), the paper provides clear information concerning the SHM system installation issues that are generally of marginal interest at laboratory scale, whereas may become relevant constraints in complex true scenarios.

Within the project SARISTU, the collected database was used to fed different damage imaging methodologies, as reported in Ref.[22] and in Ref.[23]. In this paper, the database is used in conjunction with a delay and sum beamforming

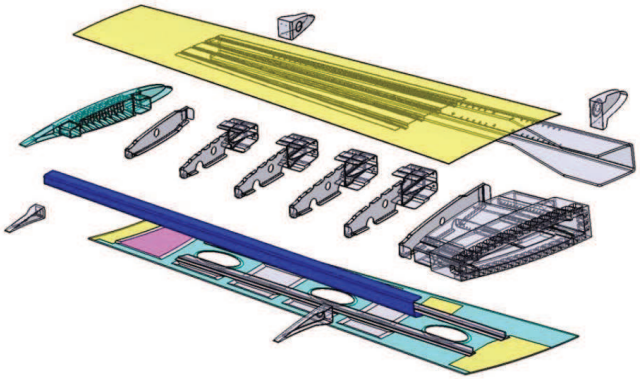


**Figure 1.** Wingbox components (courtesy of the SARISTU project[19]). The lower wing panel is highlighted in light blu colour.

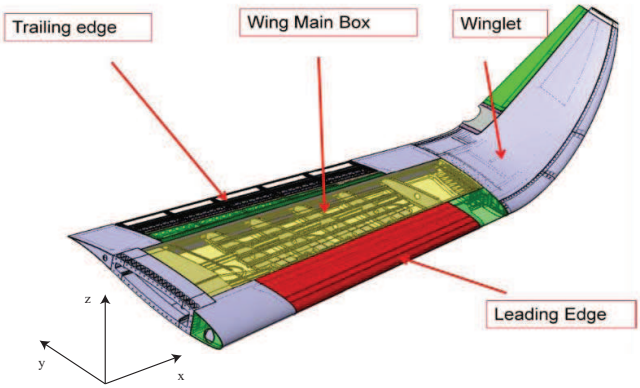



**Figure 2.** Outer wing demonstrator (courtesy of SARISTU project[19]).

algorithm, to show practically how it can be exploited. In particular, the beamforming imaging algorithm is applied on the data acquired after impacts with the aim of detecting hidden delaminations.

**Table 1.** Lower panel skin lay-up

| Ply | 6 [mm] | $\theta_i$ | 8 [mm] | $\theta_i$ | 10 [mm] | $\theta_i$ |
|---|---|---|---|---|---|---|
| 1 | 5HS | 0 | 5HS | 0 | 5HS | 0 |
| 2 | NCF | 45 | NCF | 45 | NCF | 0 |
| 3 | UN | 0 | UN | 0 | NCF | 45 |
| 4 | NCF | 0 | NCF | 0 | UN | 0 |
| 5 | UN | 0 | UN | 0 | NCF | 0 |
| 6 | NCF | -45 | NCF | 45 | NCF | 0 |
| 7 | UN | 0 | UN | 0 | UN | 0 |
| 8 | NCF | 0 | NCF | 0 | NCF | 45 |
| 9 | NCF | 0 | NCF | 0 | UN | 0 |
| 10 | UN | 0 | NCF | 45 | NCF | 0 |
| 11 | NCF | 45 | NCF | 0 | NCF | 0 |
| 12 | UN | 0 | NCF | 0 | NCF | 45 |
| 13 | NCF | 0 | UN | 0 | NCF | 0 |
| 14 | UN | 0 | NCF | 45 | NCF | 0 |
| 15 | NCF | -45 | UN | 0 | UN | 0 |
| 16 | 5HS | 0 | NCF | 0 | NCF | 45 |
| 17 | | | UN | 0 | UN | 0 |
| 18 | | | NCF | -45 | NCF | 0 |
| 19 | | | 5HS | 0 | NCF | 0 |
| 20 | | | | | UN | 0 |
| 21 | | | | | NCF | -45 |
| 22 | | | | | NCF | 0 |
| 23 | | | | | 5HS | 0 |

**Table 2.** Laminae material properties. The 1-axis coincides with the $x$-axis of the structure reference system $x-y-z$. Elastic moduli in [GPa] and mass densities in [$\mathrm{kg/m^3}$].

| Ply | $E_1$ | $E_2$ | $E_3$ | $G_{12}$ | $G_{23}$ | $G_{31}$ |
|---|---|---|---|---|---|---|
| 5HS | 65 | 65 | 8.8 | 3.6 | 3.6 | 3.6 |
| UN | 152 | 8.8 | 8.8 | 4.1 | 4.1 | 4.1 |
| NCF | 81 | 81 | 8.8 | 4.1 | 4.1 | 4.1 |

| Ply | $\nu_{21}$ | $\nu_{31}$ | $\nu_{32}$ | $\rho$ |
|---|---|---|---|---|
| 5HS | 0.041 | 0.041 | 0.041 | 1770 |
| UN | 0.018 | 0.018 | 0.31 | 1790 |
| NCF | 0.033 | 0.033 | 0.033 | 1790 |

## Database creation

### *Test Structure*

The test structure consists of a wingbox realized by assembling different carbon fiber composite components, as shown in Fig. 1. The wingbox is composed by a top panel, a lower panel, eight ribs (six central ribs, one tip rib, and one root rib), a rear spar and a front spar. The wingbox, along with the trailing edge, the leading edge and the winglet, composes the outer part of a wing demonstrator, shown in Fig. 2, that has been designed and realized within the SARISTU[19] project.

The part of the wingbox instrumented by the SHM system is the lower panel, which consists of a skin with three different nominal thicknesses ($6\,\mathrm{mm}$, $8\,\mathrm{mm}$ and $10\,\mathrm{mm}$), three man holes and two T-shape stingers. The lay-up for the three nominal thicknesses of the skin, consisting either of unidirectional Uniweave (UN) laminae, woven fabric 5-Harness (5HS) laminae or NCF-biaxial (NCF) laminae, is given in Table 1. The mechanical properties for each laminae were provided by the manufacturer (see Table 2).

A set of 133 DuraAct P876.SP1 transducers, organized in 5 main groups (A, B, C, D, E) and 8 subgroups $s_g$ (A1, A2, B, C, D1, D2, E1, E2), was bonded to the internal part of the lower wing panel (see Fig. 3). The stringers divide the lower wing panel into several bays and the sensors were positioned to cover 5 bays plus a part of two stringer foots.

Before bonding each transducer, the surface of the composite skin in contact with the transducer and a surrounding frame $3\,\mathrm{mm}$ thick was slightly sanded in order to improve the adhesion force. Abrasion dust was removed and both the substrate and the transducer bottom were cleaned with Isopropanol and let them to dry. The area around the bonding zone was covered with adhesive tape. Bi-component cold curing epoxy adhesive Hysol EA9294 by Loctite was then used to bond the transducers. A by-weight mixing ratio of 100:17 between the base and the hardener was employed. To fix the transducers in place, a normal force pressure was exerted by means of small metal counterweights, after applying the adhesive to both the substrate and the transducers bottom. The curing of the epoxy adhesive was performed at a constant temperature of $70\,^{\circ}\mathrm{C}$ obtained by means of controlled lamp heaters.

The coordinates of the sensors, and of each point of the polygonal lines describing the 8 subgroups, are available in the database as an ASCII text file.

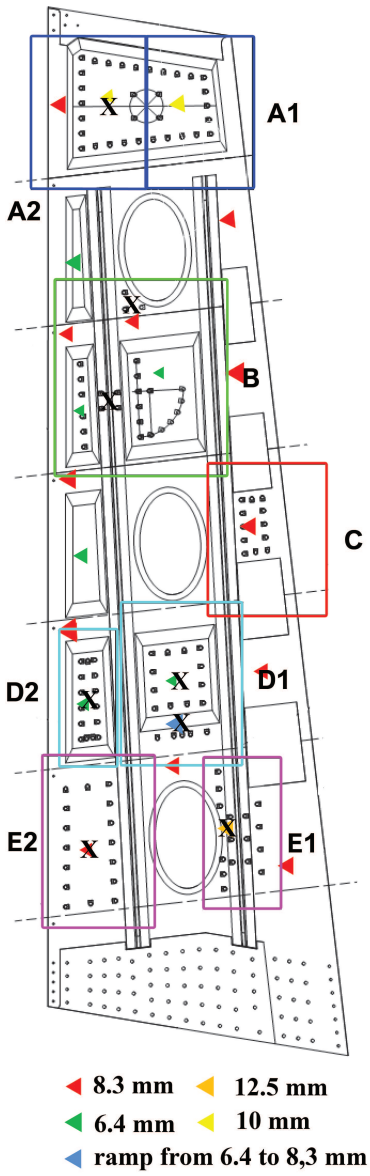



**Figure 3.** Location of the 133 transducers installed on the internal part of the lower wing panel. Transducers are grouped into 5 groups as highlighted in figure, named 'A' to 'E'. The (**X**) symbols indicate the positions of impact (described in the following) whereas the (◁) symbols indicate the measured thicknesses (courtesy of Leonardo and the SARISTU project[19]).

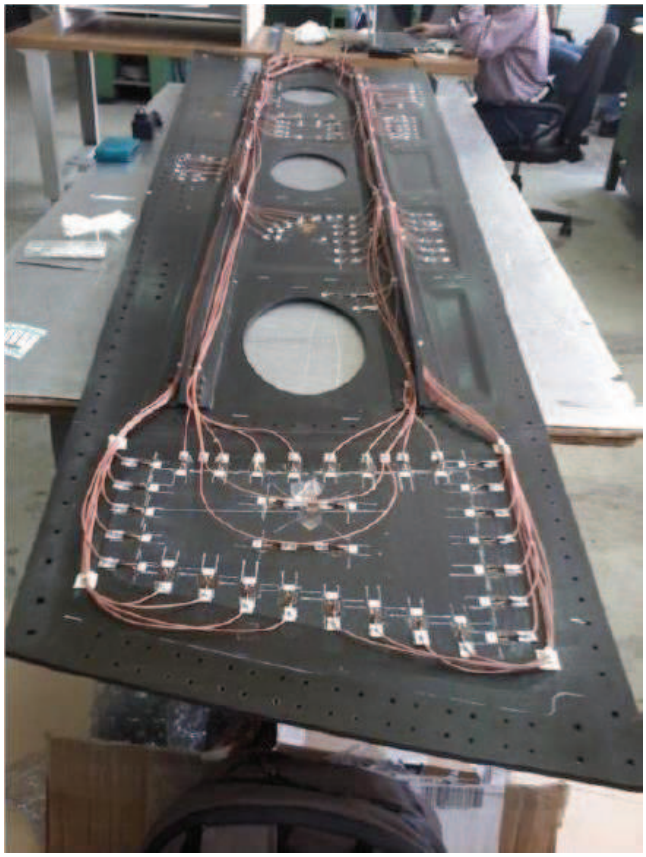


**Figure 4.** Lower wing panel with 133 transducers installed. Two bundles of cables running along the stringers are visible.

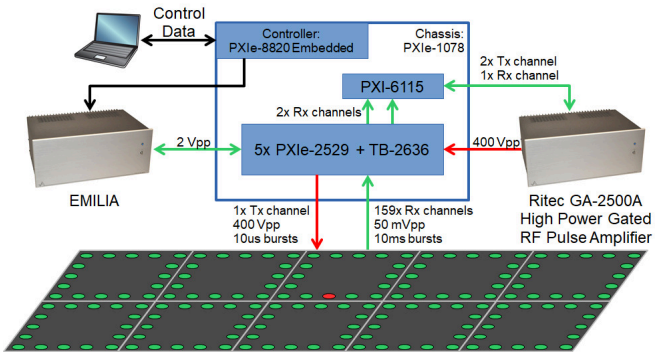



**Figure 5.** Data acquisition (DAQ) system schematic diagram.

As shown in Fig. 4, a total of 133 mini coaxial cables type RG178 (M17/93-RG178), divided into two bundles, were used to connect each sensor to the data acquisition system (DAQ). These cables are very well suited for the aeronautical environment, since they feature an operative temperature range of $-70\,^{\circ}\mathrm{C}$ to $200\,^{\circ}\mathrm{C}$, a diameter of only $1.8\,\mathrm{mm}$ and a linear density of $7.5\,\mathrm{g/m}$. They are also characterized by an attenuation of $0.085\,\mathrm{dB/m}$, an impedance of $50\,\Omega$, an inductance of $236\,\mathrm{nH/m}$, and a capacitance of $95\,\mathrm{pF/m}$. In order to minimize the cables length, as well as to increase the robustness of the experimental setup, each cable bundle was fixed along one of the two stringers of the lower wing panel.

Considering that the voltage amplitudes were designed to be in the range of $200\,\mathrm{Vpp}$ for the actuation signals, and estimated in the range of $400\,\mathrm{mVpp}$ for the reception signals, a total transmission attenuation of $6.16\,\mathrm{dB}$ and a total reception attenuation of $5.40\,\mathrm{dB}$ were estimated at the maximum frequency of $1\,\mathrm{MHz}$ and for a maximum cable length of $4\,\mathrm{m}$.

## *Data Acquisition system*

The data acquisition system (DAQ) was developed under a certain number of constraints and needs, which include: the final low cost of the DAQ, the capability to control an high number of transducers, capability to operate EMI and GW active and passive modalities and a system auto-diagnostic capability.

To tackle these instances, the DAQ system architecture shown in Fig. 5 was designed and realized. In particular, the system is composed of:

- 1 NI PXIe-1078 9-slot chassis unit;
- 1 NI controller PXIe ExpressCard 8820;

- 1 NI PXI-6115 S acquisition card;
- 5 NI PXIe-2529 switching matrix;
- 5 NI TB-2636 Screw Terminal Block;
- EMILIA: external EMI measurement device;
- RITEC: external high voltage amplifier.

The DAQ exploits LabVIEW Full Development System for Windows, it is controlled by MATLAB$^{TM}$ and it can control up to 160 piezoelectric transducers. In the following, the main components of the proposed DAQ are briefly described.

*NI PXI-6115 S acquisition card* The highest sampling frequency and the bit rate needed by the damage detection algorithms were the main constraints in the selection of the acquisition card. In particular, the chosen board has a sample rate up to $10\,\mathrm{MS/s}$, a bit rate up to $12\,\mathrm{bits}$, and the capability to perform simultaneous sampling on 4 input channels. A minimum of $16\,\mathrm{MS}$ data storage memory was also needed to cover up to $500\,\mathrm{ms}$ of recording on each channel. Hardware implemented anti-aliasing filters, with a cutoff frequency of at least $500\,\mathrm{kHz}$, were used to reduce out-of-band noise and to produce better results during the interpolation and smoothing procedures, that were carried out to produce a virtual sampling frequency of up to $100\,\mathrm{MS/s}$. On this board, a virtual bit rate of 14 bits could also be obtained by applying proper signal processing techniques.

*NI PXIe-2529 switching matrix* State of the art switching matrices have a switching bandwidth from DC to $500\,\mathrm{MHz}$. Their configuration can be determined by terminal blocks, which allow to operate multiple configurations on the same hardware. They are ideal for flexible and high-channel-count applications where signals need to be routed from different sources (like oscilloscopes, digital multimeters, arbitrary waveform generators and power supplies) to various test points on the demonstrator. The primary benefit in using a switching matrix consists in a simplified wiring, since the overall test system can easily and dynamically change the internal connections path without any external manual intervention. This capability eliminates the need to duplicate instruments and thus reducing testing cost.

In order to connect each transducer of the network to the signal generation and the DAQ, needed to automate the EMI and GW screening, five PXIe-2529 switching matrix were used. These switching matrices also allow for dynamically selecting the transducer that will act as actuator and the ones (up to 2) used as sensors. The matrices are configured to $4 \times 32$ channels, and all matrices are connected in parallel to form a single $4 \times 160$ channel matrix. The row 0 (R0) of the matrix is connected to the EMILIA device for the electromechanical impedance measurement. The rows R1 and R2 are connected to the acquisition channels of the acquisition card, and the row R3 is connected directly to the output of the high voltage amplifier.

*EMILIA* This is a device used to measure the electromechanical impedance (EMI) of one piezoelectric transducer bonded to a structure[24]. The EMI estimation approach suggests to measure the piezoelectric transducer impedance as a function of the frequency, in order to detect partial and/or total detachment of the transducer from the structure, as well as transducer malfunctioning. Specific care had to be placed to ensure the compatibility between the small signals measured by the EMILIA sensor node, and the high voltage actuation signals adopted in the guided wave measurements. As such, a dedicated sensor-near circuitry was also implemented to switch between the different measurement modalities, and to protect the EMILIA components from high voltage signals.

*RITEC* To deliver high frequency and high voltage to the piezoelectric transducers, a Ritec GA-2500A High Power Gated RF Pulse Amplifier was adopted. This one channel amplifier features an output voltage range in excess of $600\,\mathrm{Vpp}$, an output current of $3.6\,\mathrm{A}$, a slew rate of $6600\,\mathrm{V/\mu s}$ and a maximum RF Pulse Power of $400\,\mathrm{kW}$ over a full power frequency range from 30 kHz to 2.5 MHz. This instrument is well suited to drive the adopted DuraAct P-876.SP1 transducers. In using this instrument, a particular attention shall be given to the acquired signals as being the Ritec GA-2500A a gated amplifier, feed-through is expected at the opening and closing of the high power drivers. Such undesired voltages can reach up to 35 V and, in some cases, may be intense enough to excite ultrasound waves in the driven piezoelectric transducers. A proper filtering of the recorded signals mitigated this problem.

In conclusion, in the proposed architecture, the DAQ operates at most on 3 transducers at the same time. Every time it is necessary to operate a new group of transducers, the switching matrix is reprogrammed. By means of the proposed architecture, all the transducers installed in the experimental setup can be controlled by only one DAQ system, so that the entire network of transducers can be considered as a whole, and the cost of the apparatus is capped, since it is not necessary to have multiple dedicated actuating and sensing devices connected to the transducers. The DAQ is also connected to an external personal computer for remote control and data exchange during testing operations.

## Testing campaign

The EMI and the GW measurements were performed in four different testing stages, as shown in Fig. 6, namely:

1. $\mathrm{T}_0$: on the lower wing panel (LWP) before assembly the wingbox (WB);
2. $\mathrm{T}_1$: after assembly the wingbox and before fatigue testing;
3. $\mathrm{T}_2$: after fatigue testing and before impacts;
4. $\mathrm{T}_3$: after impacts.

At $\mathrm{T}_0$ EMI and GW measurements were performed on the lower wing panel resting on a table. Next, the lower wing panel was assembled together with the other parts (ribs, top panel, leading and trailing edge) to form the final wingbox. After assembly, the wingbox was hanged by means of its root rib to a previously prepared metal fixture in a cantilever configuration.

In this scenario $\mathrm{T}_1$ EMI and GW measurements were acquired.

Subsequently, the wingbox was subjected to a dedicated 90000 cycle aeronautical fatigue testing protocol via an ad hoc rig structure moved by hydraulic pistons[19]. After the completion of the fatigue protocol the $\mathrm{T}_2$ EMI and GW measurements were gathered.

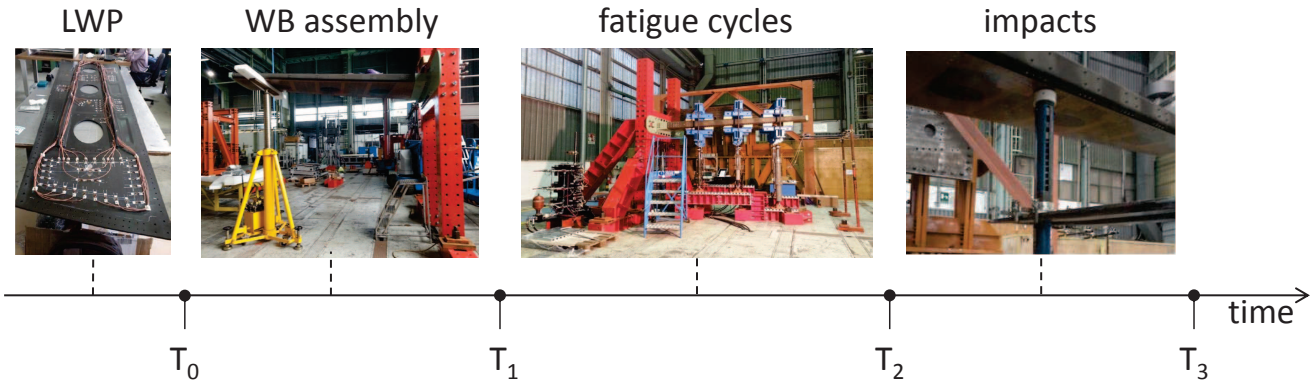



**Figure 6.** Timeline of the different $\mathrm{T_i}$ ($i = 0, 1, 2, 3$) testing phases.

Finally, the wingbox was impacted from the bottom by means of an air gun in several points, as indicated in Fig. 3, in order to generate delaminations in the lower skin panel [19]. After impacts, the $\mathrm{T_3}$ EMI and GW measurements were performed.

For each $\mathrm{T_i}$ scenario EMI measurement was performed by using EMILIA at each of the 133 transducers in the range 10 kHz to 100 kHz at 100 Hz step. The measured signals were then stored in the DAQ for further processing.

Regarding the GW screening, each transducer of each subgroup was used as actuator while the remaining transducers of the subgroup were used as sensors two at a time. Actuation form the same transducer was repeated until all the transducers of the subgroup were used as sensors. In actuation a 4.5 cycle sinusoidal wave of given central frequency $f_c$, whose amplitude was modulated my means of an Hanning window, was amplified to roughly 160 Vpp and transmitted. This pulse was able to generate guided waves propagating in the lower wing panel form the actuator to the sensors.

At $\mathrm{T_0}$, 8 different central frequencies $f_c$, namely $f_c$ =50 kHz, 60 kHz, 70 kHz, 80 kHz, 90 kHz, 100 kHz, 220 kHz and 350 kHz, were considered for the GW screening. Being the most interesting frequencies for the partners of the SARISTU project, acquisitions at $f_c =$ 50 kHz, 60 kHz and 100 kHz were repeated 10 times, in order to perform basic statistical analysis of the results, whereas only one acquisition was performed for $f_c =$ 70 kHz, 80 kHz, 90 kHz, 220 kHz and 350 kHz to keep the acquisition campaign duration within the allotted time. At $\mathrm{T_1}$, $\mathrm{T_2}$ and $\mathrm{T_3}$ a similar protocol was applied unless for the frequencies $f_c =$ 220 kHz and 350 kHz that were not considered as from $\mathrm{T_0}$ it was evident the onset of undesired multimode GW propagation.

Each GW session required 3 days, with a workload of 10 hours per day: as such, a certain amount of mismatch between the different measures was observed due to hourly and daily temperature and atmospheric pressure variations.

## The acquired database

All the collected data are freely available at the following website *http://shm.ing.unibo.it/* [25].

The recorded database comprises 5 directories, one for each testing session ($\mathrm{T_i}, i = 0, 1, 2, 3$), and one describing all the geometrical information (polygonal contour coordinates for each bay, transducers and damage locations coordinates), for a grand total of more than 120k files and 20GB of data, organized in folders to ease the localization process of the desired data.

In particular, each testing scenario $\mathrm{T_i}$ directory comprises the following sub-folders:

- *acoustic*: pitch-catch data for GW testing;
- *emiLow*: EMI data for the range 1 kHz to 20 kHz;
- *emiHigh*: EMI data for the range 20 kHz to 100 kHz;
- *speed*: pitch-catch data for group velocity estimation.

*acoustic* This folder is subdivided into several folders, one for each central frequency, which are further subdivided into subgroups and repetition folders. The leaf of this directory tree is a zip file containing the acquired GW signals in pitch-catch configuration.

*emiLow and emiHigh* These two folders contain zip files corresponding to the acquired EMI data for each sensor.

*speed* This folder is subdivided into several folders, one for each repetition of the group velocity testing. The leaf of this directory tree is a zip file containing the acquired GW in pitch-catch configuration.

Further details on the file naming and contents are available on the dedicated website [25] as a companion to the acquired data.

### Data reliability via EMI measurements

As the EMI measurement gives an indication on the integrity and bonding quality of a transducer it can be used to assess the reliability of its acquisitions for the subsequent GW screening. The output of EMILIA consists of the impedance magnitude and phase in degree for each analyzed frequency. In order to get information on sensor integrity, a parametric fitting of these two quantities is performed against a Modified Butterworth Van-Dyke (MBVD) piezoelectric transducer model [26]. This lumped model, illustrated in Fig. 7, is composed of two branches: one forms a resonant RLC tank circuit, representing the mechanical resonance contribution to the transducer impedance; the other consists of an RC series which represents the electrical contribution to the transducer impedance.

When working far from the transducer resonance frequency, the RLC tank circuit contribution is negligible and the MBVD model simplifies to an RC series circuit.

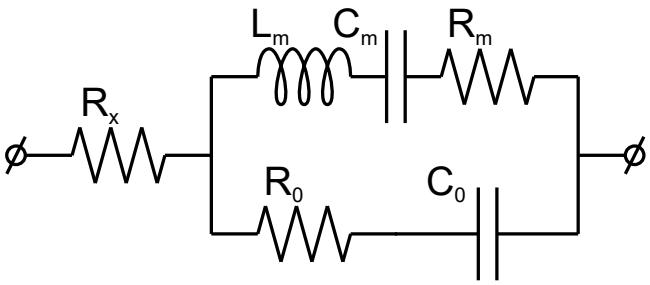



**Figure 7.** Modified Butterworth Van-Dyke (MBVD) piezoelectric transducer lumped model.

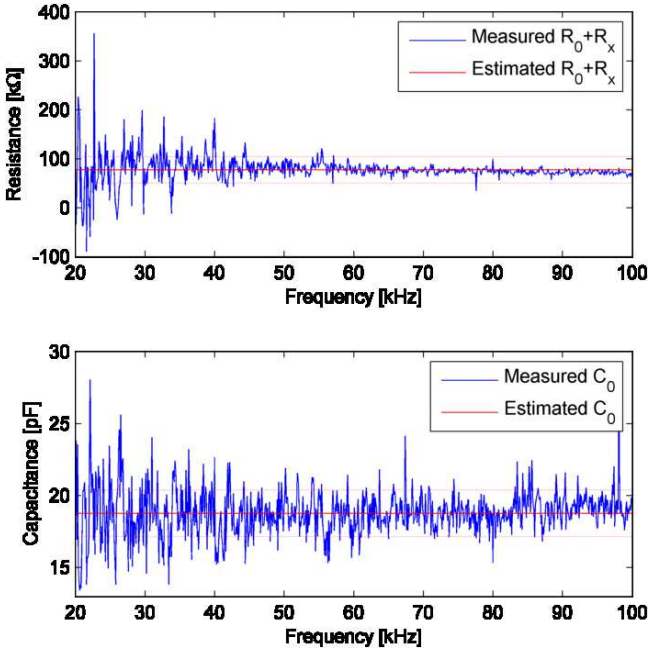



**Figure 8.** *emiHigh* measured and estimated resistive (top) and capacitive (bottom) part of the transducer impedance. Dotted lines in each graph represent the mean value plus/minus one standard deviation.

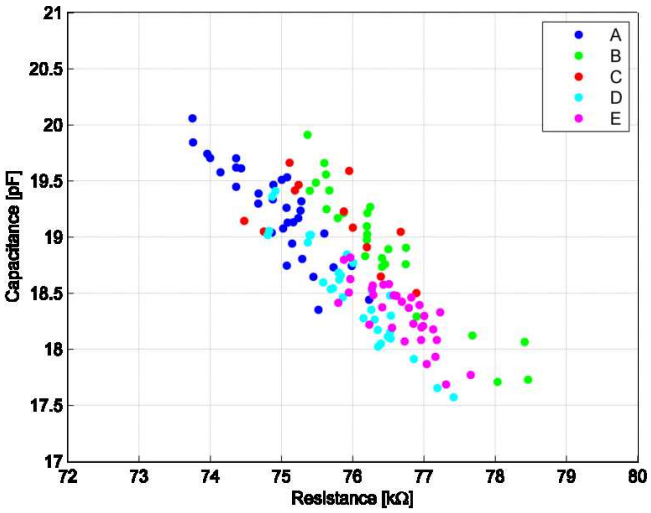



**Figure 9.** Estimated EMI values for all the 133 installed piezo transducers at $\mathrm{T}_0$. Transducers of each group, $A$ to $E$ (see Fig.3), are denoted with the same colour.

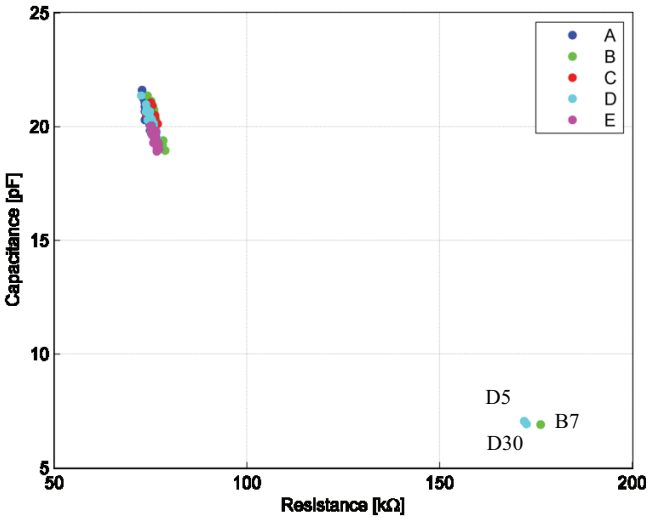



**Figure 10.** Estimated EMI values for all the 133 installed piezo transducers at $\mathrm{T}_1$. Transducers of each group, $A$ to $E$ (see Fig.3), are denoted with the same colour. Note that data for B18 is not displayed in this figure as due to a broken wire the measured capacitance was approximately 15344 pF.

Since the range of operative frequencies is $20\,\mathrm{kHz}$ to $100\,\mathrm{kHz}$, whereas the resonance frequency of the DuraAct P876.SP1 transducers is around $230\,\mathrm{kHz}$, fitting against only the RC series was performed. As such, the impedance of the transducer can be calculated as $Z(f) = (R_0 + R_x) - \jmath/(2\pi f C_0)$, so that is possible to estimate the resistive and capacitive contributions by simply separating the real part from the imaginary part of the total impedance. As shown in Fig. 8, running this simple estimation procedure for one of the 133 transducers over the range $20\,\mathrm{kHz}$ to $100\,\mathrm{kHz}$ produced results in good agreement with the measurements. In particular, the series resistance was estimated to be $R_0 + R_x = 77.2 \pm 26.6\,\mathrm{k\Omega}$, while the transducer capacitance was estimated to be $C_0 = 18.8 \pm 1.62\,\mathrm{pF}$. These values are consistent with the median resistance value of $80.0\,\mathrm{k\Omega}$ and the median capacitance of $18.6\,\mathrm{pF}$ computed over all the 133 transducers mounted on the lower wing panel.

In order to detect misbehaving sensors during the whole testing campaign (i.e. $\mathrm{T}_1$ $\mathrm{T}_2$ and $\mathrm{T}_3$) a preliminary estimation of the EMI characteristics of each sensor was performed at $\mathrm{T}_0$. As show in Fig. 9, the spread of the estimated resistance and capacitance values is contained and a significant correlation between the two parameters can be observed.

Results for the EMI acquisitions at $\mathrm{T}_1$, $\mathrm{T}_2$ and $\mathrm{T}_3$, are reported in Figs. 10, 12 and 13, respectively. At $\mathrm{T}_1$ the analyses reported that three sensors (B7, D5 and D30) and one cable (B18) were damaged during the assembly and/or the hanging of the wingbox to the metallic fixture. As shown in Fig. 10, the damaged sensors can be clearly identified by means of the R-C plot.

Moreover, by comparing the pre- and post-assembly capacitance values, as shown in Fig. 11, a distinct shift $\Delta C = 1.36\,\mathrm{pF}$ was observed. This shift is around the $8\%$ of the mean capacitance value measured during the pre-assembly EMI acquisition campaign ($\mathrm{T}_0$). According to literature the variation of piezotransducers capacitance due to temperature is around $0.25\,\%/^{\circ}\mathrm{C}$[27], which would correspond in our case to a temperature variation of $\Delta\mathrm{T} = 32\,^{\circ}\mathrm{C}$. As the highest temperature variation measured

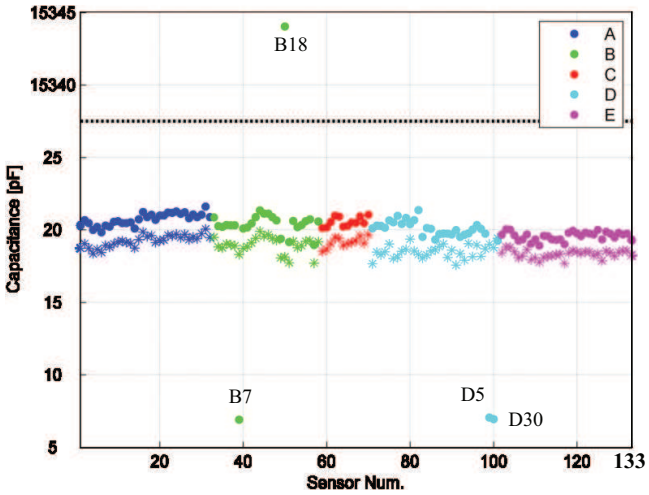



**Figure 11.** Comparison of the $T_0$ (asterisks) and $T_1$ (circles) estimated capacitance values. A distinct shift in capacitance due to structural loading and damaged sensors can be clearly identified. Transducers of each group, $A$ to $E$ (see Fig.3), are denoted with the same colour.

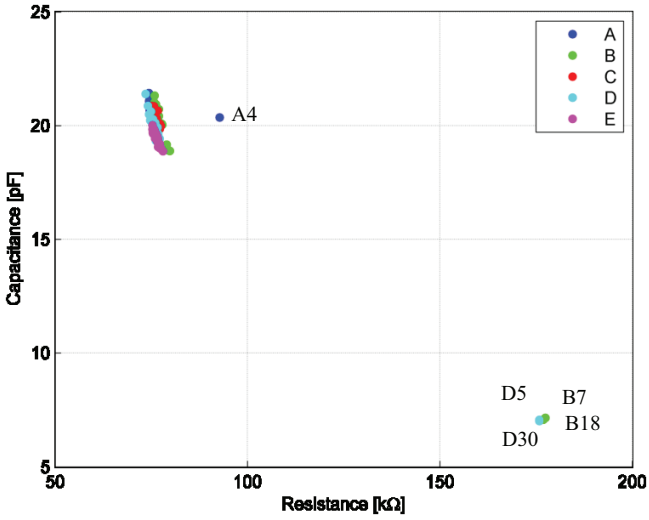



**Figure 12.** Estimated EMI values for all the installed sensors after the fatigue protocol, i.e. at $T_2$. Transducers of each group, $A$ to $E$ (see Fig.3), are denoted with the same colour.

during the experimental campaign was $\pm 5\,^{\circ}\mathrm{C}$, the shift in capacitance couldn't be attributed to a temperature variation only. Alike, as the variation of piezoelectric capacitance due to pressure variation is around $0.05\,\%/\mathrm{mbar}$[28], which would correspond to a pressure variation of $\Delta \mathrm{P} = 160\,\mathrm{mbar}$ in our case, the atmospheric pressure couldn't be considered the cause of capacitance shift as the maximum atmospheric pressure variation measured during the experimental campaign was less than $\pm 4\,\mathrm{mbar}$.

According to these considerations, we assumed that the shift in capacitance was caused by the strains and stresses generated in the lower wing panel due to the wingbox assembly as well as by the self weight of the wingbox once hanged in cantilever configuration to the metal fixture. This was also confirmed by the EMI acquisitions after fatigue cycles ($T_2$) and after impacts ($T_3$), shown respectively in Fig.12 and Fig.13, in which mean capacitance values very close to the one of $T_1$ measurements were observed.

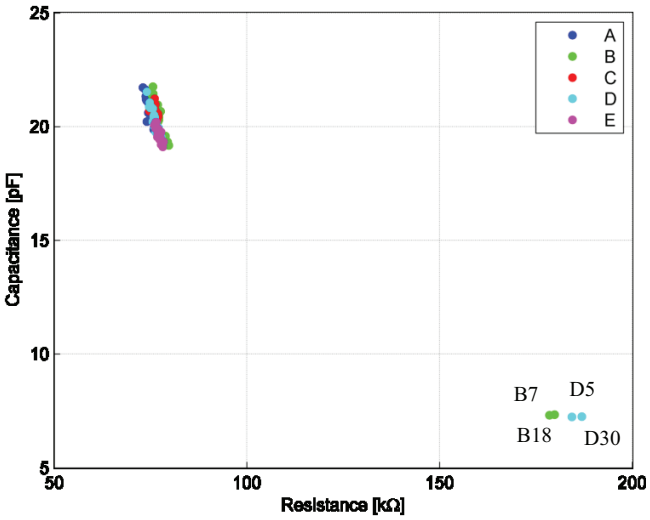



**Figure 13.** Estimated EMI values for all the installed sensors after impacts. i.e. at $T_3$. Transducers of each group, $A$ to $E$ (see Fig.3), are denoted with the same colour.

In particular, the mean capacitance shift of $T_2$ and $T_3$ with respect to the $T_1$ acquisitions is $\Delta \mathrm{C} = -0.197\,\mathrm{pF}$ and $\Delta \mathrm{C} = 0.138\,\mathrm{pF}$, respectively, which corresponds to $-0.98\%$ and $+0.69\%$. These differences are fully compatible with temperature induced variations as they would correspond to $\Delta \mathrm{T} = -3.92\,^{\circ}\mathrm{C}$ and $\Delta \mathrm{T} = 2.75\,^{\circ}\mathrm{C}$, respectively.

Concerning the effect of the fatigue cycle test, by observing Fig.12 it is possible to see that a temporary fault occurred in group A, in particular sensor A4 was involved. This fault could not have been detected by monitoring only the capacitance of the sensor as the only affected quantity was the resistance which had a shift of $17.8\,\mathrm{k\Omega}$. On the other hand, the effects of the impacts on the EMI of the piezoelectric transducers were negligible since by comparing Fig.13 with Fig.12 it can be observed that the number of faulty sensors remained the same.

In conclusion, measurements with EMILIA were able to efficiently capture transducers or cables faults, being them temporary or permanent. On the contrary, most probably due to the distance between the impacts and the transducers, it was not possible to observe any direct effect of the impact damages on the EMI measurements. Nevertheless, as discussed in Ref.[28], it was possible to detect a change in the static load of the structure by measuring the capacitance variation.

## Example of database exploitation

### *Damage imaging*

In this work a hybrid signal processing methodology, which aims at combining a wave scattering method (WSM) to a tomographic based approach method (TM), has been applied to process the GW signals. The result is a defect detection and localization algorithm that is basically wave scatter based, but makes use of tomographic baseline subtraction techniques to reduce the required amount of information concerning the geometry of wave reflectors. As the approach relies on the group velocity curves related to the propagating wave modes, dedicated measurements and processing were made to extract the group speeds (in all $0 - 360^{\circ}$ directions)

in the three thicknesses of the lower skin panel (data are available in the sub-folders *speed*).

For a given subgroup of transducers $s_g$, and for each central frequency $f_c$ of the applied pulse, the output of the hybrid approach consists in an image capable of highlighting wave reflectors within the convex hull depicted by the transducers positions.

In particular, an image is obtained by a three-step procedure:

1. *Signal preprocessing*.When dealing with a high number of transducers to be routed across a matrix of electro-mechanically controlled switches, a high cross–talk is expected and, consequently, to be removed.
   The corrupted received signal $y$ can be assumed as a linear superposition of the clean received signal to be recovered $x$, the transmitted signal waveform in the time domain $w$, and a noise component $n$:
   $$y(t) = x(t) + z(t) + n(t)$$
   $$z(t) = \mathcal{C}(t; \mathcal{D}(t; w, \mathbf{y}), k)$$
   where the following operators are defined:
   $$\mathcal{C}(t; w, k) = \max(\min(w(t), k), -k)$$
   $$\mathcal{D}(t; w, \mathbf{y}) = y_0 \cdot w(y_2 \cdot t - y_3) - y_1$$
   In these equations $k$ is the clipping parameter, whose value depends on the DAQ acquisition board settings, and $\mathbf{y} = [y_0, y_1, y_2, y_3]$ is the distortion parameter vector, which has to be numerically optimized. It is possible to recover a good estimate of the clean signal $x$ over the whole recording duration by performing the following subtraction in the time domain:
   $$\hat{x}(t) = y(t) - \mathcal{C}(t; \mathcal{D}(t; w, \hat{\mathbf{y}}), k)$$
   where:
   $$\hat{\mathbf{y}} = \underset{\mathbf{y}}{\operatorname{argmin}} \frac{1}{T} \int_0^T (y(t) - \mathcal{C}(t; \mathcal{D}(t; w, \mathbf{y}), k))^2 \, dt$$
   The resulting signal still contains noise: as such, all the parameters of the transmitted signal being known, its central frequency $f_c$ among them, a box filtering from $f_c/2$ to $3f_c/2$ is performed in the frequency domain.
2. *Time-gating*. For each transmitted signal $w_m$, after its amplitude is normalized so that $\max(|w_m|) = 1$, the time $t_{m,0}$ corresponding to the maximum of the signal envelope, computed through the Hilbert Transform absolute value, is identified; then the time duration $t_m$ of $w_m$ is computed by thresholding the envelope against a given value $w_{th}$ and a smooth windowing profile $P_m$ of the same length is generated; good results can be obtained by employing either a Chebyshev window or the envelope itself. Similarly, for each received signal $s_{m,n}$, after the *preprocessing*, the envelope is computed through Hilbert Transform absolute value. Finally, an envelope mask profile $M_{m,n}$ is constructed so that it is equal to 0 from $t = 0$ to $t_m$ and takes into account possible source images by properly replicating the $P_m$ through a suitable ultrasonic ray-tracing algorithms aware of the geometric structure of the specimen. This mask is used to compute a time–gated envelope $e_{m,n}$ by multiplying the envelope of the received signal by $1 - M_{m,n}$.
3. *Delay and sum imaging*. An elliptical beam–forming algorithm is applied to all the existing actuator-sensor processed signals (*preprocessing* and *time-gating*) for the considered subgroup of transducers.

The result of this procedure is an image in which the intensity of each point is proportional to the probability to have recorded a reflection between the direct path and the first reflection.

For instance, Figs. 14 to 20 show some results of the proposed imaging algorithm, using the open database data discussed in this work, for the post-impact scenario $\mathrm{T}_3$. In particular, Fig. 14a shows the CAD and a photo of the group A (A1 and A2) of transducers. In both pictures the position of the impact is indicated by a red star whereas the area of a C-scan, which was performed after impact, is denoted by the red box. In Fig. 14b is shown the result of the C-scan which confirms the existence of the impact induced delamination. Finally, Fig. 14c shows the result of the proposed imaging algorithm applied on the subgroup of transducers A2 for a central frequency $f_c = 50\,\mathrm{kHz}$.

Fig. 15 to Fig. 20 show similar images for the subgroups B1, C, D1, D2, E1 and E2, respectively, for a central frequency of the actuation pulse $f_c = 60\,\mathrm{kHz}$. As it can be noted the proposed algorithm properly highlights the impact positions. Of particular interest is the case for the subgroup D1 in Fig. 17 where the imaging captures both the induced delaminations one of which is in the area of the panel with changing thickness.

Further details on the impact testing protocol as well as on the C-scan testing can be found in the dedicated website[25] as well as in the Proceedings book of the SARISTU project[19].

## *Imaging based data statistic*

To assess the robustness of the images that can be computed exploiting the database, we performed a basic data analysis. For the sake of brevity, in the following we report some considerations related to all eight subgroups $s_g$ but only in correspondence of the central frequencies $f_c = 50\,\mathrm{kHz}$, $60\,\mathrm{kHz}$ and $100\,\mathrm{kHz}$.

In the testing phase $\mathrm{T}_0$, for each considered $s_g$ and $f_c$, ten GW acquisitions $n \in [1, 10] \subset \mathbb{N}$ were performed: as such 24 datasets each comprising 10 images were analyzed.

At first, for each subgroup of transducers and each central frequency, a reference image $\tilde{X}$ was obtained by calculating pixel-by-pixel the median (MED) value over $n$:
$$\tilde{X}_{i,j}(s_g, f_c) = \underset{n}{\mathrm{MED}}(X_{i,j}(s_g, f_c, n))$$
where $i, j$ are the pixel indexes. The Deviation of each image with respect to such reference image was computed as:
$$D(s_g, f_c, n) = \max_{i,j}(|X_{i,j}(s_g, f_c, n) - \tilde{X}_{i,j}(s_g, f_c)|)$$
Moreover, for each subgroup of transducers and each frequency, the difference between the minimum and maximum value of each image, hence the Range, was

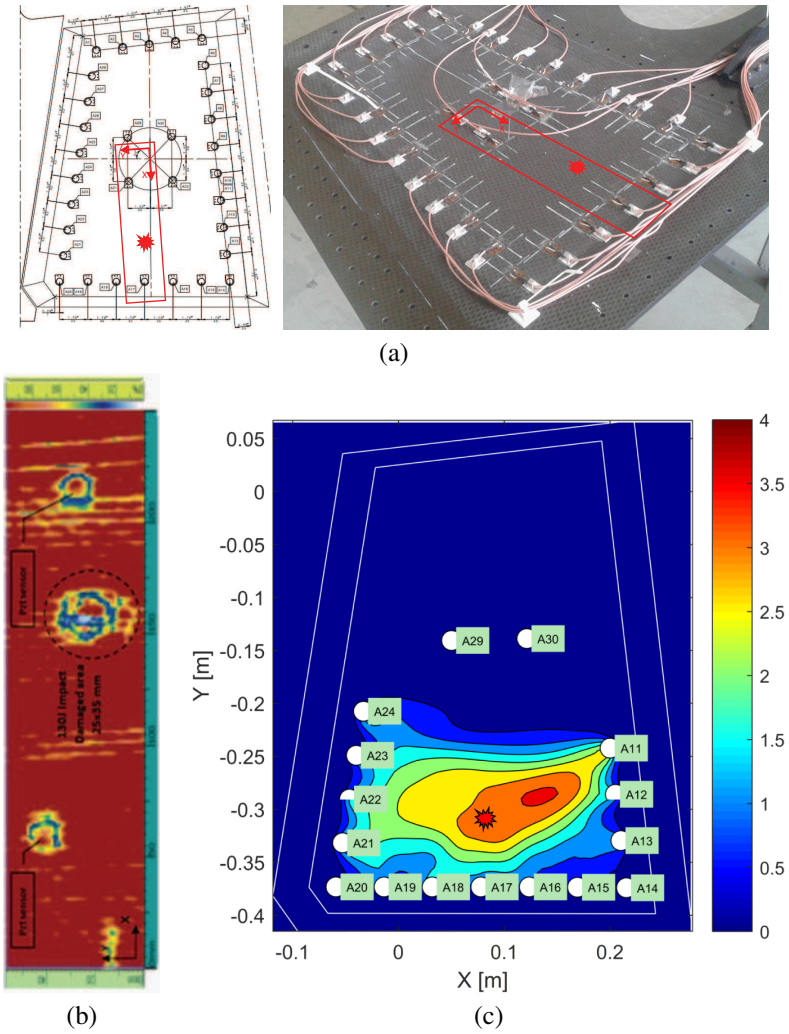



**Figure 14.** (a) CAD and image of the $A$ subgroup of transducers with highlighted the position of a $130\,\mathrm{J}$ impact (red star) and the area of the C-scan (red box). (b) C-scan image. (c) Result of the proposed imaging algorithm computed on the subgroup $A2$ of transducers and a central frequency $f_c = 50\,\mathrm{kHz}$.

calculated as:

$$R(s_g, f_c, n) = \max_{i,j}(X_{i,j}(s_g, f_c, n)) - \min_{i,j}(X_{i,j}(s_g, f_c, n))$$

Finally, the Deviation and Range are expressed through the median value of the $D$ and $R$ coefficients plus/minus their median absolute deviation (MAD) computed over $n$:

$$\text{Deviation} = \underset{n}{\mathrm{MED}}(D(s_g, f_c, n)) \pm \underset{n}{\mathrm{MAD}}(D(s_g, f_c, n))$$
$$\text{Range} = \underset{n}{\mathrm{MED}}(R(s_g, f_c, n)) \pm \underset{n}{\mathrm{MAD}}(R(s_g, f_c, n))$$

Table 3 compares Deviation and Range for each subgroup of transducers and each frequency. A robust imaging algorithm applied to a stable dataset should provide low deviations compared to the respective ranges.

As shown by Table 3, the computed images are quite stable, the maximum Deviation being less than $2\%$ than the respective maximum Range for almost all the test combinations. The same consideration applies to the MAD of the Range with respect to its mean value.

Notable exceptions are $f_c = 60\,\mathrm{kHz}$ in the subgroup A2, and $f_c = 100\,\mathrm{kHz}$ in subgroups $A1$ and $A2$: in these cases, both the maximum Deviation and the variability of the Range are larger than $12\%$ of the median range.

It can remarked here that the median operator was preferred over the mean, as, having a breakdown point of $50\%$, it is the most robust statistic. Thus, as long as no more than half of the data are contaminated the median will not give an arbitrarily large or small result. In fact, being not skewed by extremely large or small values, it is able to remove outliers even from smaller data set.

Having assessed that the median of the images obtained during $\mathrm{T}_0$ is robust, this quantity is used as a baseline reference to detect variations in the images due to external causes, that is static loading, fatigue testing and impacts. For each testing stage $\mathrm{T}_\mathrm{m}$ ($m = 1, 2, 3$), the median absolute difference over the pixels $\mathbb{E}_m(s_g, f_c, n)$, computed between the images obtained at $\mathrm{T}_\mathrm{m}$ and the corresponding reference images recorded at $\mathrm{T}_0$, is used as a damage indicator. This quantity is termed *reference error* and is obtained as:

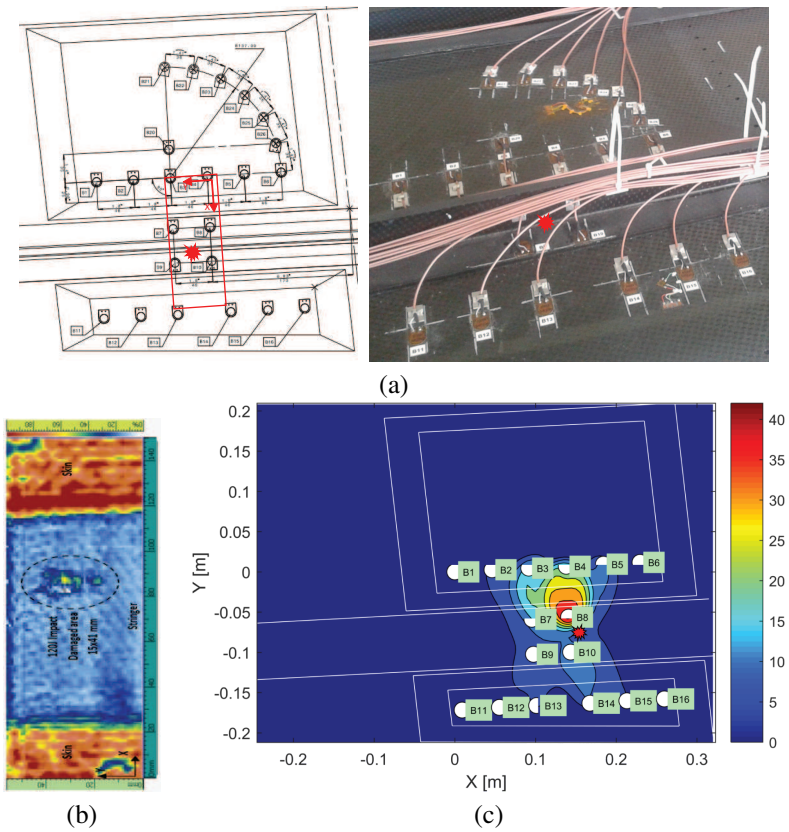



**Figure 15.** (a) CAD and image of the $B1$ subgroup of transducers with highlighted the position of a $120\,\mathrm{J}$ impact (red star) and the area of the C-scan (red box). (b) C-scan image. (c) Result of the proposed imaging algorithm computed on the subgroup $B1$ of transducers and a central frequency $f_c = 60\,\mathrm{kHz}$.

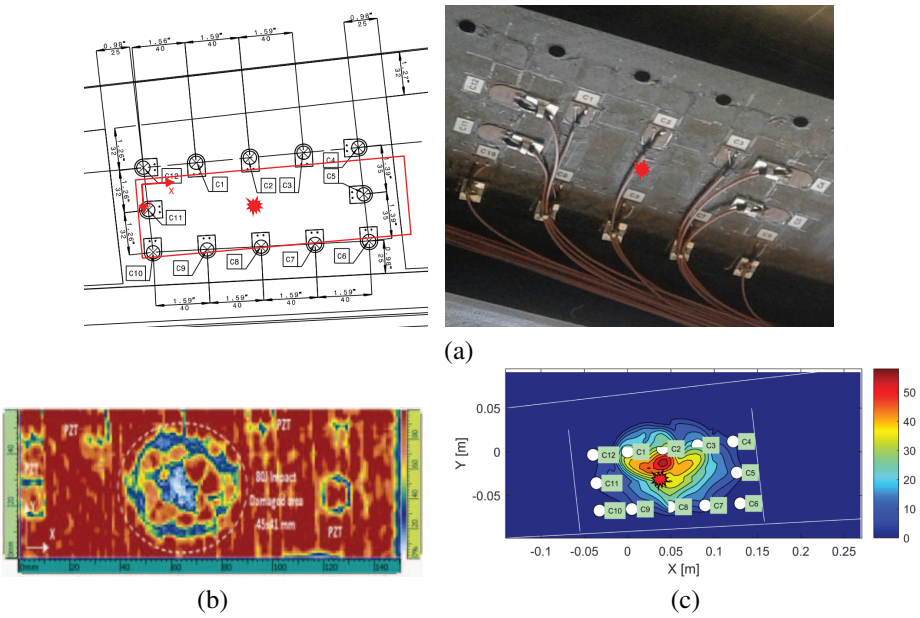



**Figure 16.** (a) CAD and image of the $C$ subgroup of transducers with highlighted the position of a $80\,\mathrm{J}$ impact (red star) and the area of the C-scan (red box). (b) C-scan image. (c) Result of the proposed imaging algorithm computed on the subgroup $C$ of transducers and a central frequency $f_c = 60\,\mathrm{kHz}$.

$$\tilde{X}^{T0}_{i,j}(s_g, f_c) = \underset{n}{\mathrm{MED}}(X^{T0}_{i,j}(s_g, f_c, n))$$
$$\Delta^{Tm}_{i,j}(s_g, f_c, n) = |X^{Tm}_{i,j}(s_g, f_c, n) - \tilde{X}^{T0}_{i,j}(s_g, f_c)|$$
$$\mathbb{E}_m(s_g, f_c, n) = \underset{i,j}{\mathrm{MED}}(\Delta^{Tm}_{i,j}(s_g, f_c, n))$$

The median value plus/minus the MAD of the reference errors computed over $n$, i.e.:

$$\mathbb{E}_m(s_g, f_c) = \underset{n}{\mathrm{MED}}(\mathbb{E}_m(s_g, f_c, n)) \pm \underset{n}{\mathrm{MAD}}(\mathbb{E}_m(s_g, f_c, n))$$

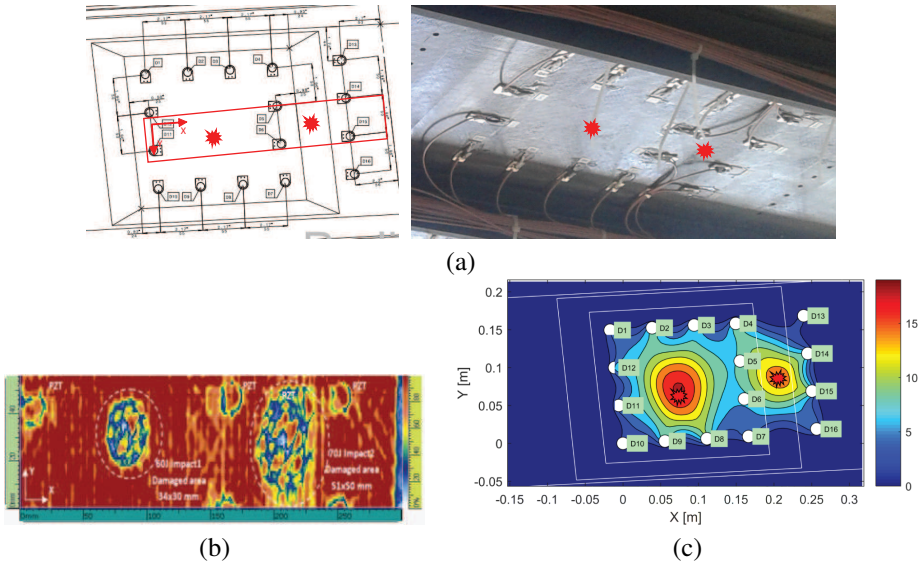



**Figure 17.** (a) CAD and image of the $D1$ subgroup of transducers with highlighted the positions of two impacts of $60\,\mathrm{J}$ and $70\,\mathrm{J}$ (red stars) and the area of the C-scan (red box). (b) C-scan image. (c) Result of the proposed imaging algorithm computed on the subgroup $D1$ of transducers and a central frequency $f_c = 60\,\mathrm{kHz}$.

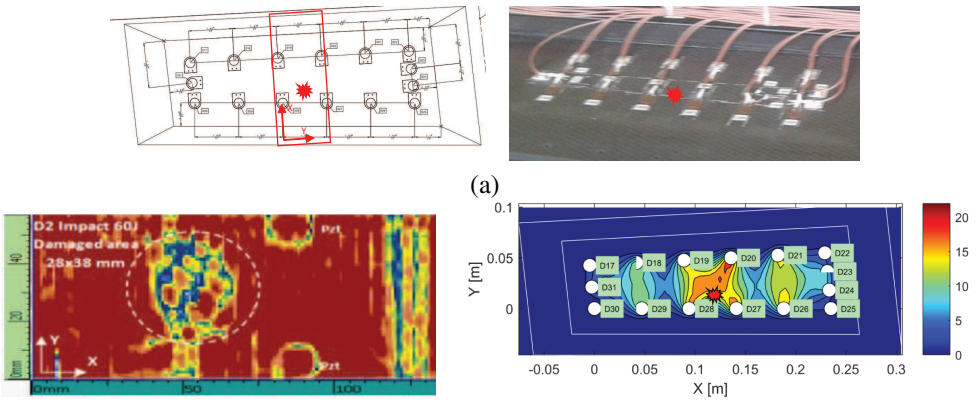



**Figure 18.** (a) CAD and image of the $D2$ subgroup of transducers with highlighted the positions of two impacts of $60\,\mathrm{J}$ (red star) and the area of the C-scan (red box). (b) C-scan image. (c) Result of the proposed imaging algorithm computed on the subgroup $D2$ of transducers and a central frequency $f_c = 60\,\mathrm{kHz}$.

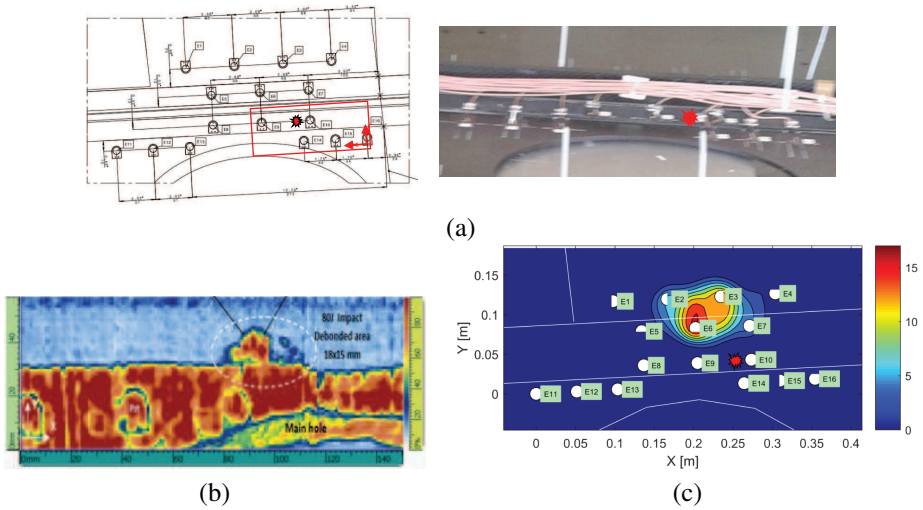
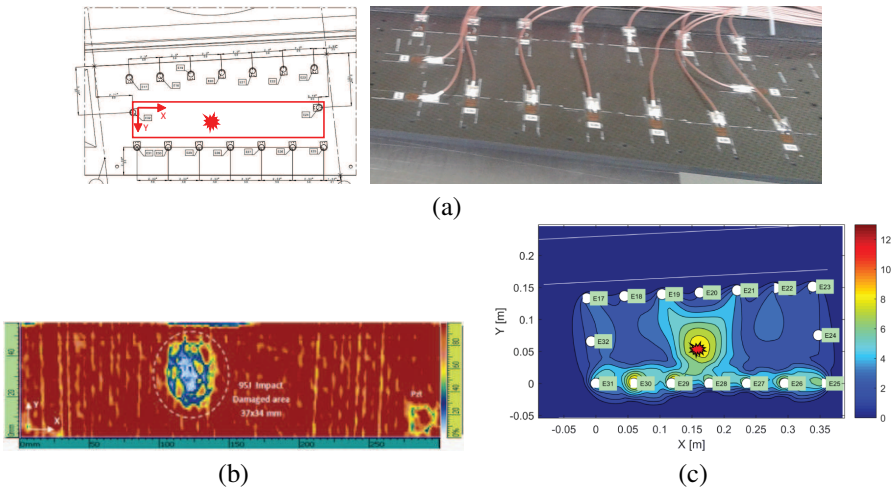



**Figure 19.** (a) CAD and image of the $E1$ subgroup of transducers with highlighted the position of a $80\,\mathrm{J}$ impact (red star) and the area of the C-scan (red box). (b) C-scan image. (c) Result of the proposed imaging algorithm computed on the subgroup $E1$ of transducers and a central frequency $f_c = 60\,\mathrm{kHz}$.




(a) (b) (c)

**Figure 20.** (a) CAD and image of the $E2$ subgroup of transducers with highlighted the impact position (red star) and the area of the C-scan (red box). (b) C-scan image for a $95\,\mathrm{J}$ impact. (c) Result of the proposed imaging algorithm computed on the subgroup $E2$ of transducers and a central frequency $f_c = 60\,\mathrm{kHz}$.

**Table 3.** Maximum absolute deviation from the median value and range for the 10 images computed for each subgroup at $\mathrm{T}_0$.

| $f_c$ [kHz] | subgroup | Deviation | Range |
|---|---|---|---|
| 50 | A1 | 0.70±0.10 | 56.40±0.30 |
| 50 | A2 | 0.60±0.20 | 44.10±0.40 |
| 50 | B1 | 1.90±0.50 | 225.30±1.30 |
| 50 | C | 1.10±0.70 | 129.20±1.10 |
| 50 | D1 | 0.30±0.10 | 24.50±0.20 |
| 50 | D2 | 1.10±5.60 | 46.10±0.60 |
| 50 | E1 | 0.80±0.50 | 81.30±0.80 |
| 50 | E2 | 1.00±1.70 | 104.90±1.90 |
| 60 | A1 | 1.50±1.20 | 81.50±0.90 |
| 60 | A2 | 0.90±10.70 | 60.60±7.70 |
| 60 | B1 | 2.70±0.50 | 303.70±1.40 |
| 60 | C | 2.90±1.00 | 267.20±2.20 |
| 60 | D1 | 0.40±0.10 | 43.50±0.10 |
| 60 | D2 | 1.00±0.60 | 70.70±0.50 |
| 60 | E1 | 0.70±0.20 | 144.40±0.40 |
| 60 | E2 | 0.80±0.20 | 180.30±0.20 |
| 100 | A1 | 2.30±34.40 | 193.60±34.90 |
| 100 | A2 | 2.00±23.30 | 131.20±23.70 |
| 100 | B1 | 7.30±2.80 | 276.10±6.30 |
| 100 | C | 7.50±1.80 | 705.40±3.50 |
| 100 | D1 | 1.90±0.40 | 89.10±0.90 |
| 100 | D2 | 4.20±1.30 | 238.40±3.00 |
| 100 | E1 | 1.70±0.40 | 183.80±0.50 |
| 100 | E2 | 3.00±0.50 | 239.60±1.40 |

is shown in Table 4, along with the information whether the computed sets from $\mathrm{T}_1$, $\mathrm{T}_2$, and $\mathrm{T}_3$ are disjoint or not.

A first consideration about these results is that, in most cases, the reference error grows along with the set number, that is, the proposed algorithm is capable to highlight a progressive change over the testing scenarios of the health status of the different bays of the lower wing panel.

More interestingly, there always exist the possibility to distinguish between the pre- and post-impact status: in fact, the best candidate frequency to operate this detection is $f_c = 60\,\mathrm{kHz}$, since in 6 cases over 8 the pre- and post-impact reference errors are disjoint and $\mathbb{E}_3$ is much greater than both $\mathbb{E}_1$ and $\mathbb{E}_2$ in all cases.

This is the best situation for a statistical classifier to operate as the number of false alarm and missed detection is the lowest. For what concerns subgroups $A1$ and $A2$, the best candidate frequency is $f_c = 50\,\mathrm{kHz}$, which reflects the results from Table 3. A possible explanation for this behavior may reside in the fact that the lower wing panel is slightly thicker in bay A than in the other bays of the panel due to the absence of stringers. Finally, it is worth noting that, among the tested frequencies, $f_c = 60\,\mathrm{kHz}$ is the only case in which all subgroups show an always growing trend, suggesting that this frequency is the best suited to perform SHM monitoring of the lower wing panel.

## Discussion and Conclusions

In this paper, an open database, collecting data from experiments on a full scale test structure realized in a carbon fiber composite, has been presented. The structure consists in the lower panel of a composite box, representing the outer part (around $4.5\,\mathrm{m}$ in length) of a regional aircraft wing, which is prone to impact damaged caused by debris during landing and take-off. The SHM system used to collect the data is based on a network of piezoelectric transducers, operating a guided waves screening for the detection of impact induced delaminations. The collected data, along with supporting explanatory files meant at guiding on its use, are free to download at the website http://shm.ing.unibo.it/.

Data have been gathered for different testing scenarios, namely on the single lower wing composite panel lying on a laboratory table in static condition ($\mathrm{T}_0$); after assembling the lower wing panel into the composite wingbox which was hanged in a cantilever configuration to a metal fixture ($\mathrm{T}_1$); after a fatigue test protocol in which the wingbox hanged on the metal fixture undergone to 90000 bending cycles ($\mathrm{T}_2$); and finally after the wingbox hanged on the metal fixture was impacted from the bottom by a controlled air gun ($\mathrm{T}_3$). The detailed description of these phases is out of the scope of

**Table 4.** Reference errors $\mathbb{E}_m(s_g, f_c)$ for each bay and each frequency over the repetitions in $\mathrm{T}_1$, $\mathrm{T}_2$, and $\mathrm{T}_3$.

| $f_c$ [kHz] | subgroup | $\mathbb{E}_1$ | $\mathbb{E}_2$ | $\mathbb{E}_3$ | $\mathbb{E}_1 \cap \mathbb{E}_2 \neq \emptyset$ | $\mathbb{E}_2 \cap \mathbb{E}_3 \neq \emptyset$ |
|---|---|---|---|---|---|---|
| 50 | A1 | 3.20±1.30 | 6.70±0.60 | 9.00±0.40 | ✓ | ✓ |
| 50 | A2 | 1.50±0.60 | 3.70±0.40 | 6.60±0.40 | ✓ | ✓ |
| 50 | B1 | 11.90±6.40 | 26.40±28.40 | 38.20±0.70 | ✗ | ✗ |
| 50 | C | 16.80±2.40 | 21.00±1.20 | 34.70±0.30 | ✓ | ✓ |
| 50 | D1 | 1.70±0.70 | 2.70±0.30 | 8.90±0.20 | ✓ | ✓ |
| 50 | D2 | 2.50±1.10 | 3.60±0.70 | 7.20±0.50 | ✗ | ✓ |
| 50 | E1 | 4.30±1.70 | 5.90±0.50 | 9.10±1.20 | ✗ | ✓ |
| 50 | E2 | 9.10±0.70 | 8.40±1.10 | 8.70±1.20 | ✗ | ✗ |
| 60 | A1 | 5.00±2.00 | 7.10±1.50 | 8.60±1.00 | ✗ | ✗ |
| 60 | A2 | 5.90±9.80 | 6.30±9.80 | 9.20±9.30 | ✗ | ✗ |
| 60 | B1 | 14.50±6.40 | 22.80±3.10 | 53.20±13.10 | ✗ | ✓ |
| 60 | C | 11.30±3.40 | 16.80±2.50 | 61.90±1.90 | ✗ | ✓ |
| 60 | D1 | 3.20±0.90 | 4.10±0.40 | 18.00±0.20 | ✗ | ✓ |
| 60 | D2 | 7.10±1.60 | 7.70±1.10 | 19.50±0.70 | ✗ | ✓ |
| 60 | E1 | 11.10±2.50 | 12.30±1.30 | 22.70±1.70 | ✗ | ✓ |
| 60 | E2 | 15.00±3.20 | 17.90±1.00 | 29.60±2.20 | ✗ | ✓ |
| 100 | A1 | 12.30±1.40 | 23.70±30.50 | 21.40±0.50 | ✗ | ✗ |
| 100 | A2 | 12.00±2.40 | 24.20±19.40 | 25.60±0.60 | ✗ | ✗ |
| 100 | B1 | 19.90±21.80 | 33.50±1.10 | 40.40±1.30 | ✗ | ✓ |
| 100 | C | 34.60±3.40 | 44.50±2.30 | 140.80±1.10 | ✓ | ✓ |
| 100 | D1 | 7.10±1.20 | 9.60±0.70 | 38.90±0.80 | ✓ | ✓ |
| 100 | D2 | 35.60±2.50 | 43.20±1.30 | 42.80±1.30 | ✓ | ✗ |
| 100 | E1 | 15.30±2.30 | 23.30±1.60 | 27.20±0.80 | ✓ | ✓ |
| 100 | E2 | 17.00±1.80 | 16.50±1.30 | 25.90±0.40 | ✗ | ✓ |

the present work and can be found in the Proceedings of the research project SARISTU[19].

As an example of its application, in this work the database has been used to feed a delay and sum damage imaging procedure with baseline subtraction. In order to compare the different test conditions and highlight trends connected to the damage mechanisms, a basic statistical analysis was performed. The results show that loading conditions and fatigue cycle clearly alter the acquired signals but the effect of impacts is much more pronounced, especially for 60 kHz signals.

Further possible investigations basing on the database include the adoption of different damage image modalities (e.g. tomographic methods), the investigation of the damage imaging performances versus the number of sensors, and the investigation of compensation procedures for the variation of loading conditions among others.

Additional metrics, besides those computed in this paper, can be analyzed to evaluate the damage imaging performances. For example, having ten acquisitions at each $f_c$ allow to estimate the component of Probability of False Alarms (PFA) due to measurement repeatability uncertainties. In particular in Ref.[29] it was demonstrated that, estimating mean value and standard deviation of a certain *damage sensitivity metric* based on a population of repeated acquisitions, it is possible to evaluate a confidence level linked to the damage statistical threshold value and to the Probability of False Alarms.

Alike, the dataset could be utilized to evaluate false alarm rates by counting the false positives detected after fatigue cycles. Such analysis would allow to estimate the so called Receiver Operating Curves (ROC) by plotting the True Positive Fraction with respect to the False positive fraction for varying detection thresholds. Moreover, additional metrics for the assessment of the defect localization performances can be considered: metrics such as the localizer operating characteristic[30] (LOC) or the cumulative probabilistic distribution function with respect to the localization error, or the evaluation of the probability of the damage to be localized (POL) within a tolerance $\varepsilon$ expressed as an absolute distance with the actual damage localization[31].

In conclusion, the proposed database does not only allow to test/validate many guided waves approaches proposed and tested so far at the laboratory scale, but also highlights pro and cons on the development of a guided waves SHM system for a full scale structure, supporting the up-scaling of guided waves based SHM systems in aeronautics.

## Acknowledgements

Mihail Lilov, Thomas Siebel and Dirk Mayer as the developers of EMILIA.

This paper is dedicated to the memory of a friend and colleague, Alfonso Apicella, who passed away on June 4, 2019. Alfonso was one of the creators of the "Smart Intelligent Aircraft Structures SARISTUS" Projects original vision. He always supported the research on Structural Health Monitoring within Italian and European academia and aeronautical industries. We will always remember his dedication to work, including the early Sunday morning phone calls, as well as his spirit that made our collaboration full of joyful moments.

## Declaration of conflicting interests

The author(s) declared no potential conflicts of interest with respect to the research, authorship, and/or publication of this article.

## Funding

The research leading to these results has received funding from the European Union's Seventh Framework Programme for

research, technological development and demonstration under grant agreement no 284562 (SARISTU Project).

## References


1. Guo N and Cawley P. The interaction of lamb waves with delaminations in composite laminates. *The Journal of the Acoustical Society of America* 1993; 94(4): 2240–2246.
2. Zhongqing S, Lin Y and Ye L. Guided lamb waves for identification of damage in composite structures: a review. *Journal of Sound and Vibration* 2006; 295: 753–780.
3. Staszewski W, Mahzan S and Traynor R. Health monitoring of aerospace composite structures–active and passive approach. *Composites Science and Technology* 2009; 69(11): 1678–1685.
4. Mitra M and Gopalakrishnan S. Guided wave based structural health monitoring: A review. *Smart Material Structures* 2016; 25(5): 053001.
5. Banerjee S, Ricci F, Monaco E et al. Autonomous impact damage monitoring in a stiffened composite panel. *Journal of Intelligent Material Systems and Structures* 2007; 18(6): 623–633.
6. Kudela P, Ostachowicz W and Zak A. Damage detection in composite plates with embedded PZT transducers. *Mechanical Systems and Signal Processing* 2008; 22(6): 1327 – 1335.
7. Yeum CM, Sohn H, Lim HJ et al. Reference-free delamination detection using lamb waves. *Structural Control and Health Monitoring* 2013; : 1–10.
8. Croxford AJ, Moll J, Wilcox PD et al. Efficient temperature compensation strategies for guided wave structural health monitoring. *Ultrasonics* 2010; 50(4-5): 517–528.
9. Harley JB and Moura JMF. Scale transform signal processing for optimal ultrasonic temperature compensation. *IEEE transactions on ultrasonics, ferroelectrics, and frequency control* 2012; 59(10): 2226–2236.
10. Dodson J and Inman D. Thermal sensitivity of lamb waves for structural health monitoring applications. *Ultrasonics* 2013; 53(3): 677–685.
11. Shubert L, Bach M, Berger U et al. Towards the deployment of acoustoultrasonics-based shm in industry. In *International workshop on structural health monitoring 2015*. pp. 2004–2011.
12. Ostiguy PC, Sherafat MH, Franca DR et al. Selection of structural features for the systematic study of guided wave propagation and interaction with damage. In *International workshop on structural health monitoring 2015*. pp. 1973–1980.
13. Galea S and Rajic N. Shm certification requirements for military aircraftan australian perspective. In *International workshop on structural health monitoring 2015*. pp. 126–133.
14. Haynes CM. *Effective Health Monitoring Strategies for Complex Structures*. PhD Thesis, University Of California, San Diego, 2014.
15. Schubert KJ, Brauner C and Herrmann AS. Non-damage-related influences on lamb wave–based structural health monitoring of carbon fiber–reinforced plastic structures. *Structural Health Monitoring* 2014; 13(2): 158–176.
16. Qiu L, Liu M, Qing X et al. A quantitative multidamage monitoring method for large-scale complex composite. *Structural Health Monitoring* 2013; 12(3): 183–196.
17. Qiu L, Yuan S, Chang FK et al. On-line updating gaussian mixture model for aircraft wing spar damage evaluation under time-varying boundary condition. *Smart Materials and Structures* 2014; 23(12): 125001.
18. Moll J, Kathol J, Fritzen CP et al. Open guided waves: online platform for ultrasonic guided wave measurements. *Structural Health Monitoring* 2018; 0(0): 1–12.
19. Wolcken P and Papadopoulos ME. *Smart Intelligent Aircraft Structures (SARISTU): Proceedings of the Final Project Conference*. Springer International Publishing, 2015.
20. Flynn EB and Todd MD. A Bayesian approach to optimal sensor placement for structural health monitoring with application to active sensing. *Mechanical Systems and Signal Processing* 2010; 24: 891–903.
21. Yi TH, Li HN and Zhang XD. A modified monkey algorithm for optimal sensor placement in structural health monitoring. *Smart Materials and Structures* 2012; 21(10): 105033.
22. Ricci F, Monaco E, Lecce L et al. Guided waves for detection of delamination and disbonding in stiffened composite panels. In *Proc. SPIE*, volume 9438. pp. 94380P–94380P–7.
23. Hettler J, Tabatabaeipour M, Delrue S et al. Linear and nonlinear guided wave imaging of impact damage in cfrp using a probabilistic approach. *Materials* 2016; 9(11): 901.
24. Lilov M and Siebel T. EMILIA – a compact impedance analyzer for local integrity assessment. In *Structural Dynamics. EURODYN 2014. Proceedings of the 9th International Conference on*. pp. 2173–2177.
25. shm.ing.unibo.it. SARISTU open database, 2018. URL `http://www.shm.ing.unibo.it`.
26. Larson JD, Bradley PD, Wartenberg S et al. Modified butterworth-van dyke circuit for fbar resonators and automated measurement system. In *Ultrasonics Symposium, 2000 IEEE*, volume 1. IEEE, pp. 863–868.
27. Davoudi S. *Effect of Temperature and Thermal Cycles on PZT Ceramic Performance in Fuel Injector Applications*. PhD Thesis, Department of Mechanical & Industrial Engineering University of Toronto, 2012.
28. Ozeri S and Shmilovitz D. Static force measurement by piezoelectric sensors. In *2006 IEEE International Symposium on Circuits and Systems*. pp. 5179–5182.
29. Memmolo MLBNMERF V. Damage detection tomography based on guided waves in composite structures using a distributed sensor network. *Optical Engineering* 2016; 55(1): 011007–1–11.
30. Flynn EB, Todd MD, Wilcox PD et al. Maximum-likelihood estimation of damage location in guided-wave structural health monitoring. *Proceedings of the Royal Society A: Mathematical, Physical and Engineering Sciences* 2011; 467(2133): 2575–2596.
31. Moriot J, Quaegebeur N, Le Duff A et al. A model-based approach for statistical assessment of detection and localization performance of guided wave–based imaging techniques. *Structural Health Monitoring* 2018; 17(6): 1460–1472.